Threshold photoionization and density functional theory studies of bimetallic-carbide nanocrystals and fragments: Ta_3ZrC_y (y=0–4)

V. Dryza[a] and G. F. Metha[b]
Department of Chemistry, The University of Adelaide, South Australia 5005, Australia

(Received 21 December 2008; accepted 26 May 2009; published online 23 June 2009)

Gas-phase bimetallic tantalum-zirconium-carbide clusters are generated using a constructed double ablation cluster source. The Ta_3ZrC_y (y=0–4) clusters are examined by photoionization efficiency spectroscopy to extract experimental ionization energies (IEs). The IE trend for the Ta_3ZrC_y cluster series is reasonably similar to that of the Ta_4C_y cluster series [V. Dryza *et al.*, J. Phys. Chem. A **109**, 11180 (2005)], although the IE reductions upon carbon addition are greater for the former. Complementary density functional theory calculations are performed for the various isomers constructed by attaching carbon atoms to the different faces of the tetrahedral Ta_3Zr cluster. The good agreement between the experimental IE trend and that calculated for these isomers support a $2\times2\times2$ face centered cubic nanocrystal structure for Ta_4ZrC_4 and nanocrystal fragment structures for the smaller clusters. © *2009 American Institute of Physics*. [DOI: 10.1063/1.3154384]

I. INTRODUCTION

Investigations of several group IV and V transition metal-carbide clusters (M_xC_y) in the gas-phase have lead to the discovery that geometrically closed face centered cubic (fcc) "nanocrystals" are among the most favorable structures formed, e.g., $2\times2\times2$ M_4C_4 and $3\times3\times3$ $M_{14}C_{13}$.[1,2] The structures of these metal-carbide nanocrystals in their neutral states have been verified by correlating the absorption features obtained via infrared-resonance enhanced multiphoton ionization (IR-REMPI) spectroscopy with the phonon modes of bulk fcc metal-carbide (100) surfaces obtained via electron energy loss spectroscopy.[3–5] Furthermore, these experiments established the high stability of the nanocrystals as the IR-REMPI technique relies on ionization of a cluster upon adsorption of multiple IR photons rather than fragmentation.

As bulk fcc metal-carbide is utilized for its superior ability to catalyze certain chemical reactions, such as hydrodesulfurization,[6] metal-carbide nanocrystals in this size range may display enhanced catalytic behavior due to the greater number of exposed metal atoms and size-dependent electronic structures.[7,8] Given that metal-carbide nanocrystals are preferentially formed by both group IV and V metals, the transition from, for example, $Ti_{14}C_{13}$ to $V_{14}C_{13}$ by sequential substitution of metal atoms would be expected to maintain the geometric structure and integrity of the electronic structure. However, this substitution would alter the population and perturb the energies of the molecular orbitals (MOs). This creates the fascinating possibility of constructing group IV/V bimetallic-carbide nanocrystals, with their properties tailored for novel nanotechnological applications.

Experimental studies on bimetallic-carbide clusters have only been performed by Castleman and co-workers[9–11] on the M_8C_{12} "met-car," a structure possessing quite different bonding motifs to nanocrystals. The met-car contains six C_2 units bound across the six butterfly motifs created by the underlying tetracapped tetrahedron M_8 cluster and is a very stable structure for a range of group IV and V transition metals.[2,5] In one study they determined the ionization energies (IEs) of the $Ti_{8-x}Zr_xC_{12}$ clusters (where x=0–4 and 8) by photoionization efficiency (PIE) spectroscopy.[11] It was found that the IE of Ti_8C_{12} (4.40 eV) is higher than that of Zr_8C_{12} (3.95 eV), with the IEs of the bimetallic met-cars decreasing continuously as the number of substituting Zr atoms increased.

Poblet and co-workers[12] utilized density functional theory (DFT) to computationally examine a range of the bimetallic met-cars, including the $Ti_{8-x}Zr_xC_{12}$ (x=0–5 and 8) clusters experimentally generated by Cartier *et al.*[10] Two isomers were considered for each $Ti_{8-x}Zr_xC_{12}$ cluster, where the metal atom present in the lowest concentration appeared in either all the inner or outer tetrahedral positions, respectively. The difference in energy between the two isomers was found to be very small (never exceeding 0.065 eV), indicating that substitution was not favored toward either of the two metallic positions. These calculations explained the regular statistical distribution of peaks in the nascent $Ti_{8-x}Zr_xC_{12}^+$ mass spectrum, which had initially been interpreted as evidence that all eight of the metal atoms were located in symmetry-equivalent positions.[10]

In contrast to bimetallic met-cars, investigations of bimetallic-carbide nanocrystals have been limited to a single computational study by Ivanovskaya *et al.*[13] on the $3\times3\times3$ $Ti_{13}XC_{13}$ cluster, where X was various first row transition metal atoms. They found that Sc and V substitution affected the electronic structure the least, with the substituted atoms involved in similar MOs to those of the replaced Ti atom.

[a]Present address: School of Chemistry, The University of Melbourne, Victoria 3010, Australia.
[b]Author to whom correspondence should be addressed. Department of Chemistry, The University of Adelaide, South Australia 5005, Australia. Tel.: +61 8 8303 5943. FAX: +61 8 8303 4358. Electronic mail: greg.metha@adelaide.edu.au.

Our group has previously conducted an experimental and computational examination of the Ta_4C_y $(y=0-4)$ clusters,[14,15] the results of which supported the $2\times2\times2$ nanocrystal structure of Ta_4C_4 determined via IR-REMPI spectroscopy.[4] In this paper we report the generation of bimetallic tantalum-zirconium-carbide clusters of the form Ta_xZrC_y using a double ablation cluster source. The Ta_3ZrC_y $(y=0-4)$ clusters are examined by a combination of PIE spectroscopy and DFT calculations. The predicted nanocrystal structure of Ta_3ZrC_4 and nanocrystal fragments for the smaller clusters are supported by the good agreement between the experimental IE trend and theory. Although substitution of a Ta atom with a Zr atom in the Ta_4C_y clusters preserves the clusters' geometry, modifications in the electronic structure are highlighted.

II. EXPERIMENTAL AND COMPUTATIONAL METHODS

A. Experimental

The double ablation source used to generate the bimetallic-carbide clusters is similar to that described by Nonose *et al.*[16] It has two metal rods ($\phi=2$ mm) displaced by a distance of 5 mm along the gas channel in the ablation cap. The two rods are situated at opposite sides of the gas channel and ablated by independent 532 nm laser pulses (~6 mJ/pulse). Both rods are rotated and translated by the same screw mechanism motor in conjunction with a gear mechanism. For the generation of the tantalum-zirconium-carbide clusters presented herein, the Ta rod was held in the rod position closest to the output of the pulsed nozzle, with the Zr rod positioned downstream. However, the Zr rod was ablated ~7 μs earlier than the Ta rod; this procedure will be described in detail in Sec. III A.

The remaining details of the laser ionization experiment are identical to that reported previously.[15] A gas mix consisting of 0.02% acetylene seeded in helium, introduced by the pulsed nozzle, is reacted with the ablation products and passed along a 15 mm long "condensation tube" before undergoing expansion into the first vacuum chamber of the time-of-flight mass-spectrometer (TOF-MS). The clusters pass via a homebuilt skimmer into the second chamber that contains a standard Wiley–McLaren TOF-MS arranged perpendicularly with the cluster molecular beam. The neutral clusters are ionized with the frequency-doubled output of a Nd:YAG-pumped dye laser. The resultant ions are detected by a double multichannel plate detector, amplified $\times125$ (Stanford SR445) and the signal sent to a digital oscilloscope (LeCroy 9350 AM, 500 MHz) for averaging (1000 laser shots) before being saved on a PC for analysis. All data points are collected at 0.25 nm intervals. Due to inefficiencies in the dye laser grating near 425 nm (Wood's anomaly), data points between 210 and 214 nm are recorded using the first anti-Stokes output from a Raman-shifter operating with H_2. Typical laser powers used are 50 μJ/pulse, collimated to a 5 mm diameter beam, as measured using a power meter (Ophir PE10BB). During each PIE scan, the laser power is kept constant. To check that long term intensity fluctuations in the cluster source had not occurred, the laser is returned to the starting wavelength immediately after each scan to ensure that the cluster signal intensity remains constant.

B. Computation

Geometry optimization and harmonic vibrational frequency calculations were performed using DFT in the GAUSSIAN 03 suite of programs.[17] Calculations employed the B3P86 method with the Stuttgart/Dresden (SDD) basis set. Yang *et al.* found simulated pulsed field ionization–zero electron kinetic energy (PFI-ZEKE) spectra based on the structures and vibrational frequencies calculated from the B3P86 method reproduce the features of the experimental spectra for the benchmark metal-carbide clusters Nb_3C_2 and Y_3C_2.[18] We have previously calculated the lowest energy isomers of the Ta_4C_y $(y=0-4)$ clusters using the B3P86 method with the LANL2DZ basis set.[15] We found that repeating the calculations with the SDD basis set led to almost identical structures and relative energies.

All Ta_3ZrC_y isomers were initially optimized without any geometry constraint. The minimized isomers were then examined to determine any symmetry properties and the calculations were repeated within the highest symmetry point group. The symmetry-constrained energy was subsequently compared to the unconstrained energy to ensure that there was no difference. All isomers were characterized with vibrational frequency calculations to determine whether the optimized structure was a true minimum. Calculations were conducted at the two lowest spin multiplicities (i.e., $2S+1=2$ and 4 for the neutral and 1 and 3 for the cation). In all cases, the spin expectation values $\langle S^2\rangle$ were within 10% of the theoretical value. The adiabatic IEs were calculated as the energy difference between the neutral and cationic ground states, including zero-point energies (ZPEs). All details (i.e., geometric, atomic charges and energy information) for both the neutral and cationic isomers are contained in the supplementary material.[19]

All presented geometries of the cluster isomers have bonds drawn between the metal atoms if their distance is less than, or equal to, the covalent radius of the two metal atom combined, i.e., Ta–Ta$\leq$2.76 Å and Ta–Zr$\leq$2.86 Å. Metal-carbon bonds are drawn at bond lengths less than or equal to 2.35 Å. Atomic charges were determined by natural bond order (NBO) calculations.[20] MOs are drawn at an isoelectric potential of 0.05 a.u.

III. RESULTS AND DISCUSSION

A. Generation of tantalum-zirconium-carbide clusters

The primary difficulty in generating bimetallic-carbide clusters composed of Ta and Zr atoms is that they have similar m/z values compared with the monometallic-carbide clusters, thus making spectroscopic measurements difficult. This overlap occurs because the mass of a Zr atom (isotope pattern: ^{90}Zr 51.45%, ^{91}Zr 11.22%, ^{92}Zr 17.15%, ^{94}Zr 17.38%, and ^{96}Zr 2.80%) is approximately half that of a Ta atom (^{181}Ta 99.99%). For example, Ta_xZrC_y clusters will overlap with larger $Zr_{2x+1}C_y$ clusters. This overlap is likely to be present even under single-photon ionization conditions, as

the Zr_xC_y and $Ta_xZr_zC_y$ clusters are expected to have IEs in a similar energy range to that of the Ta_xC_y clusters.[15,21,22]

Initial generation of Ta-rich bimetallic-carbide clusters was attempted with the Ta rod ablated first on the leading edge of the gas pulse, with the Zr rod (located downstream) ablated after a ~6 μs time delay. However, this procedure did not generate Ta_xZrC_y clusters in a greater concentration than the overlapping Zr_xC_y clusters (see supplementary material[19]). By changing the relative timing of the ablation lasers so that the Zr rod is ablated ~7 μs *earlier* than the Ta rod (using identical timing of the pulsed nozzle), Ta_xZrC_y clusters are generated in substantial concentration and without having interference from large Zr_xC_y clusters.

By applying this procedure, it was found that the distribution of the cluster species changes in different regions in the molecular beam, allowing the Ta_xZrC_y clusters to be isolated by adjusting the timing of the ionization laser. Figures 1(a)–1(e) show mass spectra obtained by changing the timing of the ionization laser (220 nm) by 10 μs increments. Time zero (0 μs) is arbitrarily set to that used when recording PIE spectra (it is ~300 μs after ablation of the Ta rod). The mass spectrum at −30 μs [Fig. 1(a)] predominately consists of Zr_xC_y clusters. The spectrum at −20 μs [Fig. 1(b)] also primarily consists of Zr_xC_y clusters, but now a new large peak appears at m/z of 567 due to Ta_3C_2. At −10 μs [Fig. 1(c)] there is a decrease in Zr_xC_y clusters, but an increase in Ta_xC_y clusters is observed. Furthermore, the peaks in the m/z region of the Ta_xZrC_y (x=3–5) clusters have become sharper, indicating that these peaks are now bimetallic-carbide clusters rather than Zr_xC_y clusters, i.e., the latter are broader due to the combinations of the Zr atom isotopes. The next mass spectrum at 0 μs [Fig. 1(d)] primarily consists of Ta_xC_y clusters and Ta_xZrC_y (x=3–5) clusters. Interestingly, bimetallic-carbide clusters of the form Ta_2ZrC_y are not observed with any great intensity most likely because their IEs are greater than the photon energy available at 220 nm. The last mass spectrum at +10 μs [Fig. 1(e)] predominantly consists of Ta_xC_y clusters, with small amounts of Ta_xZrC_y clusters still present.

Further confirmation for the mass assignments of the peaks assigned to the Ta_xZrC_y (x=3–5) clusters is that these peaks are not present when each metal rod is stopped being ablated separately at the 0 μs ionization laser time.[19] Ablation of only the Zr rod generates very weak amounts of Zr_xC_y (x=1–2) clusters, which are believed not to be ionized by a single photon at the laser energy used.

It is not immediately apparent as to why ablating the Ta rod before the Zr rod (first ablation procedure) does not generate substantial Ta_xZrC_y clusters, whereas ablating the Ta rod after the Zr rod (second procedure) does. Since the Ta_xZrC_y peaks disappear instantaneously when ablation of the Zr rod is stopped, deposition of Zr species on the Ta rod cannot be the reason. In the first ablation procedure we postulate that the Ta rod is ablated on the leading edge of the gas pulse, which carries the ablated products toward the Zr rod, with initial Ta_xC_y cluster generation occurring in this time. When the Zr rod is ablated, the majority of the Ta_xC_y clusters are dissociated, creating an abundance of Ta atoms and also an abundance of Zr atoms. This generates large amounts of

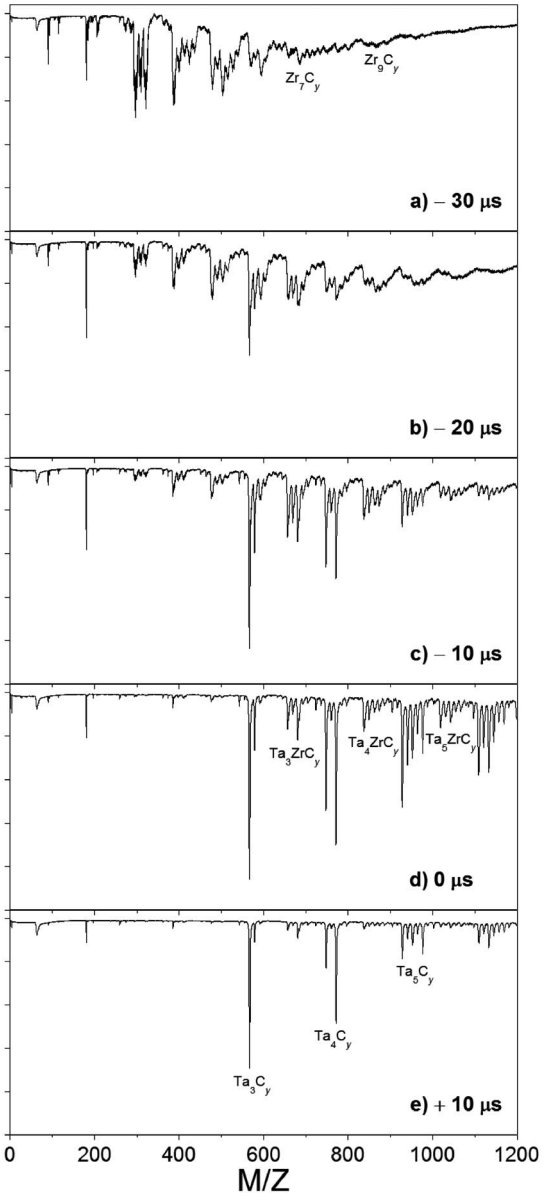

FIG. 1. Mass spectra of ionized neutral clusters generated by the ablation of the Zr rod ~7 μs earlier than the Ta rod (see text for details).The spectra differ by the timing of the ionization laser: (a) −30 μs, (b) −20 μs, (c) −10 μs, (d) 0 μs, and (e) +10 μs (where 0 μs is arbitrarily set to the optimum delay for generating the Ta_3ZrC_y clusters; see text for details).

Ta_xC_y and Zr_xC_y clusters and a small amount of Ta_xZrC_y clusters. Furthermore, this procedure leads to an essentially uniform distribution of the clusters in the molecular beam.

In the second ablation procedure we postulate that the Zr rod is ablated before the leading edge of the gas pulse has reached this area. The ablation products then expand in both directions of the gas channel, and in the absence of abundant bath gas, they remain as mostly atomic species. The Ta rod is then ablated ~7 μs later on the leading edge of the gas pulse. As the ablated Ta products are carried downstream, generating initial Ta_xC_y clusters as they proceed, they encounter and overlap a small portion of the Zr atoms traveling in the opposite direction. There will be a region of overlap volume where the Ta atoms and Ta_xC_y clusters are in much greater concentration than the Zr atoms so that Ta_xC_y and

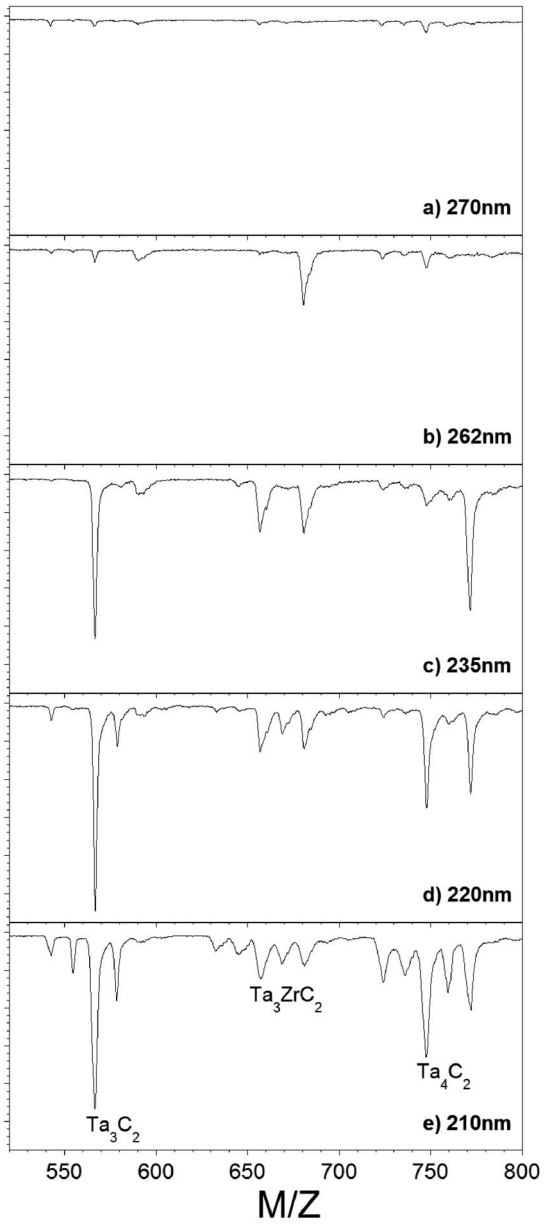

FIG. 2. Mass spectra of Ta_3C_y, Ta_3ZrC_y, and Ta_4C_y clusters at five different ionization wavelengths: (a) 270 nm, (b) 262 nm, (c) 235 nm, (d) 220 nm and (e) 210 nm.

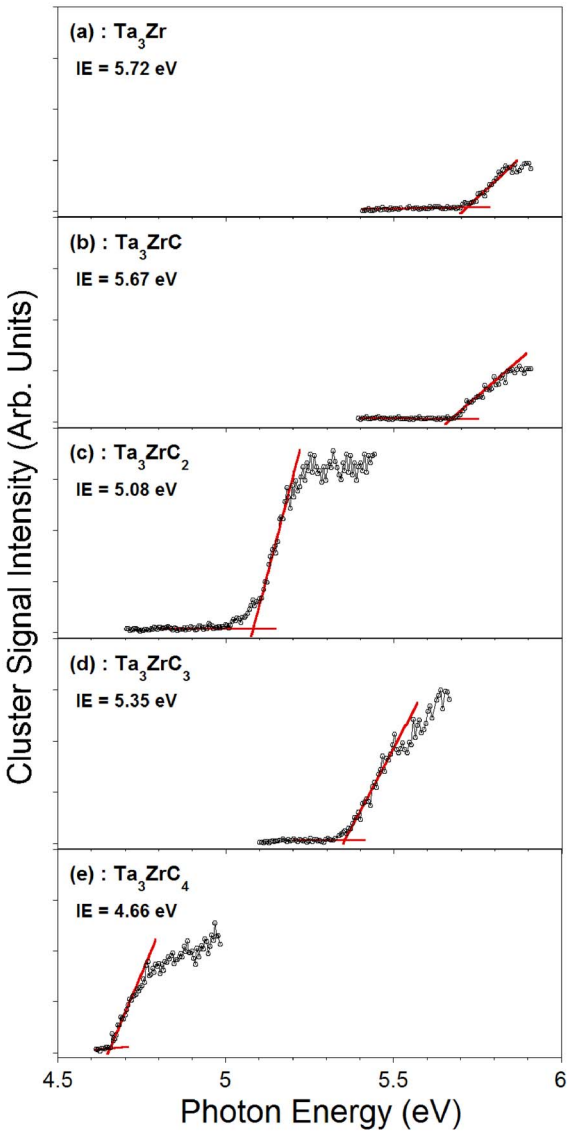

FIG. 3. (Color online) PIE spectra for the Ta_3ZrC_y ($y=0-4$) clusters. The determined IEs are also displayed.

Ta_xZrC_y clusters are primarily generated rather than large Zr_xC_y clusters. By adjusting the timing of the ionization laser [Figs. 1(a)–1(e)], this specific region of the molecular beam can be investigated [Fig. 1(d)].

B. PIE Experiments

All PIE spectra are collected for the Ta_3ZrC_y ($y=0-4$) clusters with the Zr rod ablated 7 μs before the Ta rod (i.e., the second ablation procedure) and the 0 μs laser ionization time [i.e., Fig. 1(d)]. Figures 2(a)–2(e) show a portion of the mass spectra for clusters generated from the double ablation source following single-photon ionization at five different wavelengths (270, 262, 235, 220, and 210 nm) collected under otherwise identical conditions. In the spectrum recorded at 210 nm [Fig. 2(e)] clusters containing Ta_3Zr appear with zero to four C atoms attached, with the Ta_3ZrC_2 cluster having the greatest intensity.

The spectrum recorded at 270 nm [Fig. 2(a)] shows only baseline levels, as none of the species are ionized with one photon. At 262 nm [Fig. 2(b)] Ta_3ZrC_4 is ionized, the first bimetallic-carbide cluster to appear. Ionization at 235 nm [Fig. 2(c)] results in Ta_3ZrC_2 appearing, followed by Ta_3ZrC_3 at 220 nm [Fig. 2(d)]. Finally back at 210 nm [Fig. 2(e)], Ta_3Zr and Ta_3ZrC are now ionized.

PIE spectra are recorded by monitoring the signal of each cluster as a function of photon energy. PIE spectra for the Ta_3ZrC_y ($y=0-4$) clusters are shown in Figs. 3(a)–3(e). The cluster Ta_3ZrC_2 has a slightly steeper rising slope from its baseline level, relative to the other clusters, indicating good Franck–Condon overlap between the ground electronic state geometries of the neutral and cation. For all spectra two lines are fitted, one to the baseline and one to the linear rise of signal, and their intersection defined as the IE (with an estimated error of ± 0.05 eV). Although the ionization pro-

cess is vertical, since little geometry change is observed between the neutral and cationic ground states for these clusters (*vide infra*) the onsets of ionization are considered to be good approximations to the adiabatic IEs. It should be noted that extracting the vertical IEs from PIE spectra (i.e., locating the maximum of the first derivative of the increasing ion signal) of metal containing clusters is possible and has been performed previously, although in this study the ion signal was normalized for cluster source fluctuations.[23] The vibrational temperature of the clusters is estimated to be ~300 K as the extracted IEs of Nb_3C_2 and Nb_5C_2 in our previous studies were found to be only slightly lower (<0.04 eV) than the adiabatic IEs determined via PFI-ZEKE photoelectron spectroscopy.[22,24,25]

The IE values determined for all the Ta_3ZrC_y (y=0–4) clusters are displayed in the PIE spectra and are also tabulated later. For the Ta_3ZrC_y series, relative to the IE of Ta_3Zr, addition of one C atom only reduces the IE very slightly (0.05 eV). Addition of two and three C atoms causes large (0.64 eV) and intermediate (0.37 eV) IE reductions, respectively. A substantial IE reduction of 1.06 eV is observed for addition of four C atoms.

C. DFT calculated isomers

In our previous study of the Ta_4C_y (y=0–4) clusters, the isomers assigned to the ionization onsets are based on a $2\times2\times2$ nanocrystal structure for Ta_4C_4, with the smaller clusters formed by loss of C atoms (i.e., they are nanocrystal fragments).[15] Although gas-phase Zr_4C_y clusters have been observed previously,[26] no experimental or computational studies exist on Zr_4C_y (y=1–4).

For each Ta_3ZrC_y (y=0–4) cluster DFT calculations were performed on all possible isomers generated by replacing a Ta atom with a Zr atom in the corresponding Ta_4C_y cluster that we have reported previously.[15] This procedure is considered appropriate for two reasons. First, the neutral Ta_3ZrC_y clusters are isoelectronic with cationic Ta_4C_y clusters, and we have previously shown that the same structural isomers are the lowest in energy for both neutral and cationic Ta_4C_y clusters. Second, a previous combined experimental and computational study on anionic V_xO_y clusters has shown that substitution of V atoms (group V) with Ti atoms (group IV) does not alter the proposed polyhedral cage structures.[27]

All the isomers considered for the *neutral* Ta_3ZrC_y (y=0–4) clusters are shown in Fig. 4. The relative energies (ΔE in eV) for each isomer of a cluster are also given in the figure. Similar geometric minima for each isomer were also identified on the *cationic* surface.

The accuracy of the relative energetics from the DFT calculations is expected to be <0.3 eV. This value is estimated by the energy changes observed for the Nb_xC_y isomers (without carbon-carbon bonding) by extending the SDD basis set on the C atoms to an aug-cc-pVTZ basis set[24,25] and a separate study correlating the experimental properties of the most abundant Nb_9 isomer with DFT calculations.[28]

DFT calculations have shown that Zr_4 has a slightly distorted tetrahedral geometry of high spin $[^7A', C_s]$,[29] whereas our calculations on Ta_4 give an ideal closed-shell tetrahedron

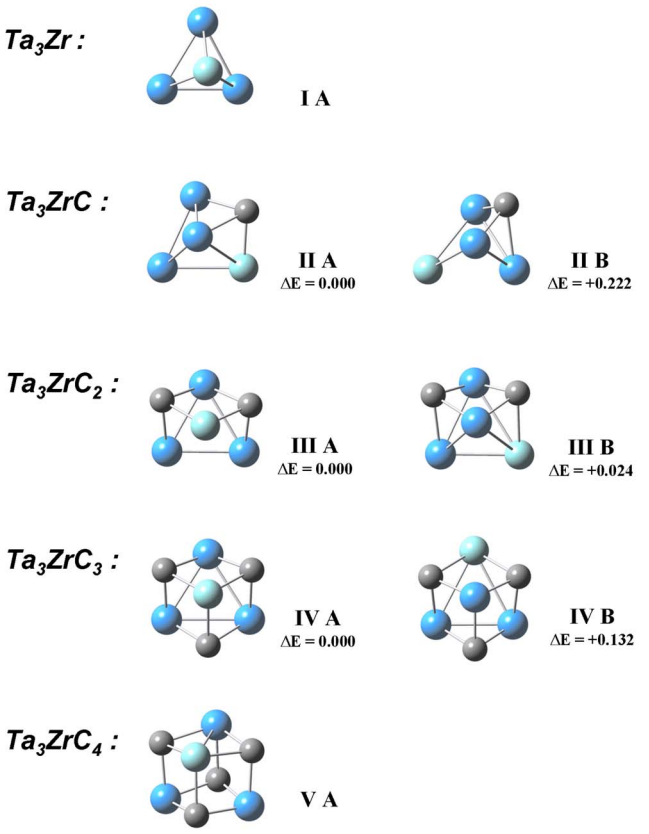

FIG. 4. (Color online) Structures of calculated isomers for the neutral Ta_3ZrC_y (y=0–4) clusters. Written beneath each isomer are the relative energies (ΔE in eV).

$[^1A_1, T_d]$. The latter result is in agreement with Raman studies of Ta_4 in a rare-gas matrix.[30] Here, we find a distorted tetrahedron of low spin to be the lowest energy structure for Ta_3Zr (**I A**$[^2A', C_s]$). Note the symmetry of Ta_3Zr **I A** is C_s rather than the ideal C_{3v} symmetry, consistent with Ta_4^+ being C_{2v} rather than T_d symmetry due to Jahn–Teller distortion. Of the four metal faces available on Ta_3Zr **I A** there are three faces containing two Ta atoms and one Zr atom (denoted "Ta_2Zr face"), with the one remaining face containing all Ta atoms (denoted "Ta_3 face"). It is also worth noting that a recent computational investigation of the Nb_3Zr cluster by our group found the lowest energy structure to also be a distorted tetrahedron with doublet multiplicity.[31]

Two isomers are possible for Ta_3ZrC: either with the C atom bound to a Ta_2Zr face (**II A**$[^2A, C_1]$) or the Ta_3 face (**II B**$[^2A', C_s]$) of the tetrahedral Ta_3Zr cluster. The former isomer is the lowest in energy by 0.222 eV.

Two isomers are possible for Ta_3ZrC_2. One has the two C atoms bound to separate Ta_2Zr faces (**III A**$[^2A, C_1]$), and the other has one C atom bound to a Ta_2Zr face and another C atom bound to the Ta_3 face (**III B**$[^2A'', C_s]$). The former is only very slightly lower in energy (ΔE=+0.024 eV).

Similarly, two isomers are possible for Ta_3ZrC_3. The lowest in energy is that where all the C atoms are bound separately to all three available Ta_2Zr faces of the tetrahedral Ta_3Zr cluster (**IV A**$[^2A', C_s]$). The other has two C atoms bound to two Ta_2Zr faces, and the remaining C atom bound to the Ta_3 face (**IV B**$[^2A'', C_s]$) and is 0.132 eV higher in energy.

TABLE I. List of experimental IEs (reported in eV) observed for the Ta_3ZrC_y (y=0–4) clusters. Also listed are DFT calculated transitions and IEs, excluding ZPE, including ZPE, and offset IE (i.e., $IE^{\dagger}$).

Cluster	Expt. IE	Isomer	Calc. transition	Calc. IE (exc. ZPE)	Calc. IE (inc. ZPE)	Calc. $IE^{\dagger}$
Ta_3Zr	5.72	I A	$^3A'' \leftarrow {}^2A'$	5.832	5.840	5.720
Ta_3ZrC	5.67	II A	$^1A' \leftarrow {}^2A$	5.659	5.679	5.559
		II B	$^1A' \leftarrow {}^2A'$	5.844	5.846	5.726
Ta_3ZrC_2	5.08	III A	$^1A' \leftarrow {}^2A$	5.493	5.516	5.396
		III B	$^1A' \leftarrow {}^2A''$	5.747	5.762	5.642
Ta_3ZrC_3	5.35	IV A	$^3A' \leftarrow {}^2A'$	5.974	5.977	5.857
		IV B	$^3A'' \leftarrow {}^2A''$	5.731	5.742	5.622
Ta_3ZrC_4	4.66	V A	$^1A'' \leftarrow {}^2A'$	5.145	5.167	5.047

Only one isomer for Ta_3ZrC_4 (**V A** [$^2A', C_s$]) is possible by substituting a Ta atom with a Zr atom in the $2\times2\times2$ nanocrystal isomer of Ta_4C_4, i.e., C atoms are bound to all the available metal faces on the tetrahedral Ta_3Zr cluster. Note that **V A** has C_s rather than the ideal C_{3v} symmetry. Indeed, our calculations show that the isoelectronic $Ta_4C_4^+$ has D_{2d} symmetry rather than the ideal T_d symmetry.

D. Comparison between calculated and experimental IEs

Adiabatic ionization transitions are considered for all the isomers for each Ta_3ZrC_y cluster, following the $\Delta S = \pm 1/2$ rule for ionization. Only IEs including ZPEs are considered for discussion. These IEs are listed for the Ta_3ZrC_y (y =0–4) clusters in Table I, in addition to the experimental values.

It is seen that the absolute calculated IEs for all the Ta_3ZrC_y isomers are higher than the experimental values. In our previous investigations of the Nb_xC_y (x=3–5) clusters, the B3P86 method in conjunction with the SDD basis set on the metal atoms was also observed to systematically overestimate the experimental IEs.[24,25] Despite this overestimation the IE changes upon sequential addition of C atoms to a bare metal cluster consistently matched the experimental trend.

When the IEs of the Ta_4C_y (y=0–4) clusters were recalculated using the current computational method, they also overestimated the experimental values, although they are constantly lower by ~0.2 eV than those calculated with LANL2DZ basis set.[15] This indicates that the B3P86 method has a greater influence in the IE overestimation than the smaller basis set contraction or effective core potential of the LANL2DZ basis set.

As this study has also determined the IEs following sequential addition of C atoms to a bare metal cluster, the change in IE relative to the Ta_3Zr cluster is considered. A linear offset of −0.120 eV is applied to the IEs of the Ta_3ZrC_y isomers so that the calculated and experimental IE values of Ta_3Zr coincide. This approach has been shown to be effective in our previous studies on other metal-carbide clusters containing from three to five metal atoms.[15,24,25] The offset IE of each isomer, herein referred to as $IE^{\dagger}$, is given in the final column of Table I and is also plotted in Fig. 5 along with the experimental IE for that cluster.

The calculated $IE^{\dagger}$s of the Ta_3ZrC isomers **II A** and **II B** are both quite close to the experimental value with deviations of −0.111 and +0.056 eV, respectively. Therefore, the experimental IE is assigned to **II A** as it is the lowest energy isomer.

Although the two isomers of Ta_3ZrC_2 **III A** and **III B** are essentially equal in energy, they exhibit sufficiently different $IE^{\dagger}$s. The lowest energy isomer (**III A**) is assigned to the ionization onset as its calculated $IE^{\dagger}$ is in much better agreement with the experimental value than that of the low-lying isomer (i.e., deviations of +0.316 and +0.562 eV, respectively).

The deviations between the calculated $IE^{\dagger}$s and experimental value for the **IV A** and **IV B** isomers of Ta_3ZrC_3 are +0.507 and +0.272 eV, respectively. This deviation for the lowest energy isomer (**IV A**) is beyond what we consider to be an acceptable deviation from the experimental IE. Since the low-lying isomer **IV B** has an $IE^{\dagger}$ in good agreement with the experimental value and is only 0.132 eV higher in energy than **IV A**, we assign it to the ionization onset. It should be noted that this is the only metal-carbide cluster (both isomers) for which the lowest cationic state is a triplet, rather than a singlet, which can be accessed from the doublet neutral state.

The substituted $2\times2\times2$ nanocrystal (**V A**) of Ta_3ZrC_4 has a calculated $IE^{\dagger}$ in reasonable agreement with the experimental IE (a deviation of +0.387 eV). As there is only one possible isomer generated via the considered substitution

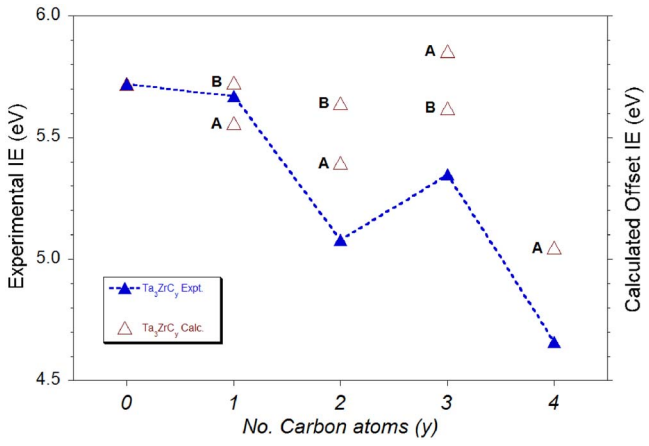

FIG. 5. (Color online) Graph showing experimental IE values for the Ta_3ZrC_y clusters as a function of y. Also shown on the same scale are the offset values, $IE^{\dagger}$, calculated using DFT. The letters (**A** and **B**) denote the isomers for that particular cluster (see text for details).

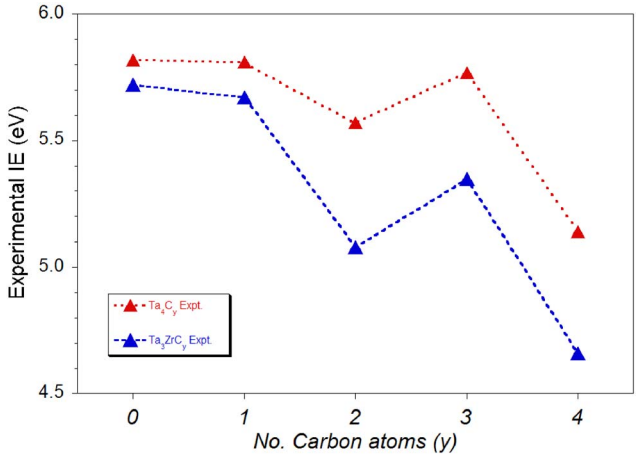

FIG. 6. (Color online) Graph showing experimental IE values for the Ta_4C_y (Ref. 15) and Ta_3ZrC_y clusters as a function of y.

procedure, this deviation gives some indication of the maximum uncertainty of our calculated $IE^{\dagger}$ values relative to experiment.

E. Relative energetics of the Ta_3ZrC_y cluster isomers

Substitution of a Ta atom with a Zr atom in the clusters examined here shows that substitution does not have substantial preference for either of the two different metallic positions available in the Ta_3ZrC_y (y=1–3) nanocrystal fragments, with the energy difference for the two isomers varying between 0.024 and 0.222 eV (i.e., below the expected accuracy of the DFT calculations). However, Zr atom substitution consistently favors the metal atom position that facilitates the C atoms always being bound to the Ta_2Zr faces of the tetrahedral Ta_3Zr cluster, leaving the Ta_3 face unbound.

From the NBO charge analyses for all the Ta_3ZrC_y isomers (see supplementary material[19]), the Zr atom has a greater positive charge than the equivalent Ta atom in the corresponding Ta_4C_y cluster. Indeed, the Zr atom has a small positive charge in the bare Ta_3Zr cluster, with all the Ta atoms possessing slight negative charges. This is consistent with the Zr atom having a lower electronegativity than the Ta atom (1.33 cf. 1.50 on the Pauling scale). In the lowest energy isomers of the Ta_3ZrC_y (y=1–3) clusters, the Zr atom is always bound to all the electronegative C atoms. The Zr atom possesses a greater positive charge in these isomers compared to those higher in energy. Therefore, the favored Zr–C bonding compared to Ta–C bonding is most likely due to the slightly greater ionic bonding component of the Zr–C interaction.

F. Comparison of IE trends for the Ta_3ZrC_y and Ta_4C_y clusters

The experimental IEs for both the Ta_3ZrC_y and Ta_4C_y clusters are plotted in Fig. 6 as a function of the numbers of C atoms attached. The IEs of Ta_3Zr and Ta_3ZrC are slightly reduced from those of Ta_4 and Ta_4C (0.09 and 0.15 eV, respectively). However, the IEs of Ta_3ZrC_2, Ta_3ZrC_3, and Ta_3ZrC_4 are all reduced by relatively larger amounts: 0.50, 0.40, and 0.47 eV, respectively. The observed lowering of the IEs when a Zr atom substitutes a Ta atom is consistent with the fact that the Zr atom has a lower IE than Ta (6.66, cf. 7.89 eV).[32]

Overall, the IE trend for the Ta_3ZrC_y cluster series is broadly similar to that of the Ta_4C_y cluster series, as clusters containing two and four C atoms have the greatest IE reductions relative to the bare metal clusters.[15] However, there is a distinct difference in the two IE trends for clusters containing three C atoms. In the Ta_4C_y cluster series the IE of Ta_4C_3 is very similar to that of Ta_4 and Ta_4C, whereas in the Ta_3ZrC_y cluster series the IE of Ta_3ZrC_3 is appreciably reduced compared to that of Ta_3Zr and Ta_3ZrC. Here Ta_3ZrC_3 is the only cluster where the low-lying isomer (i.e., **B**) has a lower IE than the lowest energy isomer (i.e., **A**), and is calculated to be only 0.132 eV higher in energy. Since the threshold ionization technique favors the detection of the isomer present with the lowest IE (i.e., ionization onsets of the higher IE isomers are not discernable in the PIE spectra), it is possible that both isomers of Ta_3ZrC_3 are present in our experiment. Therefore, the IE trends of the Ta_3ZrC_y and Ta_4C_y cluster series may be very similar if the ionization onset of isomer **A** for Ta_3ZrC_3 was measured and used in the data set instead of isomer **B**.

G. Influence of Zr substitution on the electronic structure of Ta_4C_3 and Ta_4C_4

The above results suggest that the geometries of the Ta_3ZrC_y (y=0–4) clusters are maintained upon substitution of a Zr atom into the corresponding Ta_4C_y cluster, and the similar energy of the **A** and **B** isomers for Ta_3ZrC_y (y=1–3) also indicates that the bonding of the Zr and Ta atoms is comparable. However, whether the substitution results in changes to the electronic structure is less clear. To investigate this, the electronic structures and frontier MOs are compared for (i) the $2\times2\times2$ nanocrystal Ta_3ZrC_4 and its isoelectronic analog $Ta_4C_4^+$ and (ii) the C-deficient nanocrystal fragment Ta_3ZrC_3 and its nonsubstituted analog Ta_4C_3.

High electronic and geometric stabilities have been proposed for the $2\times2\times2$ M_4C_4 nanocrystals constructed from group IV and V transition metals.[4,8,33] It is therefore reasonable to expect that Ta_3ZrC_4 also possesses these properties and, as such, warrants further investigation. The electronic structure and the frontier MOs of the isoelectronic $Ta_4C_4^+$ are shown in Fig. 7(a). There is a large energy difference between the HOMO and HOMO−1 relative to the remaining occupied MOs, as the former are Ta–Ta bonding/nonbonding and the latter primarily Ta–C bonding in character. The LUMO to LUMO+2 are Ta–Ta antibonding/nonbonding in character. These frontier MOs have appreciable nonbonding character as indicated by the relatively long Ta–Ta/Ta–Zr bond lengths (~2.9 Å) and the small HOMO-LUMO gap (~1.7 eV) for $Ta_4C_4^+$. The electronic structure and the frontier MOs of Ta_3ZrC_4 are shown in Fig. 7(b), and there are significant rearrangements compared to the isoelectronic $Ta_4C_4^+$. The LUMO and LUMO+1 of Ta_3ZrC_4 have significantly less Zr character than expected compared to the corresponding MOs in $Ta_4C_4^+$. More significantly, the LUMO in $Ta_4C_4^+$ is now the HOMO in Ta_3ZrC_4. Overall these differ-

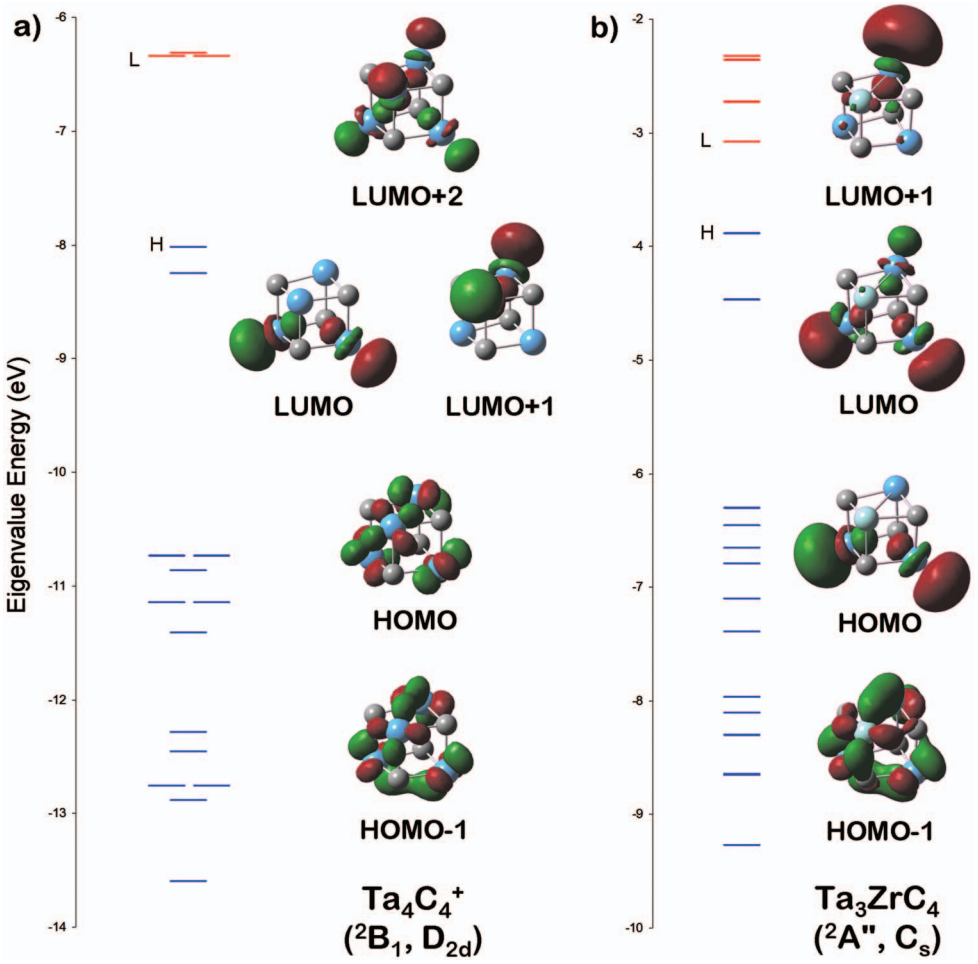

FIG. 7. (Color) Calculated energy level diagrams for the (a) $Ta_4C_4^+$ and (b) Ta_3ZrC_4 clusters. The occupied (unoccupied) orbitals are in blue (red) with the HOMO and LUMO labeled by H and L, respectively. Pictures of the frontier MOs are also shown.

ences indicate a reduction in the number of "nonbonding" electrons delocalized over the metal atoms in Ta_3ZrC_4, relative to Ta_4C_4.

The lone free metal face available in the C-deficient $2\times2\times2$ nanocrystal fragment (M_4C_3) presents itself as a potential site for chemical reactions to occur. In our previous study of the isovalent Nb_4C_y clusters,[24] the lowest energy structure of Nb_4C_5 was found to have a C_2 unit attached to the free Nb_3 face of Nb_4C_3. The lowest energy structure of Nb_4C_6 on the neutral surface was found to contain two C_2 units, yet on the cationic surface it has a C_3 unit attached to the free Nb_3 face of $Nb_4C_3^+$. This latter example indicates markedly different reactivity of a group V M_4C_3 cluster when one electron is removed. Figure 8(a) shows the electronic structure and the frontier MOs of Ta_4C_3. The HOMO to HOMO−2 are Ta–Ta bonding across the free Ta_3 face and its edges and are quite similar in energy. Like that observed for $Ta_4C_4^+$, the remaining occupied MOs are much lower in energy due to their Ta–C bonding character. The LUMO is nonbonding in character and localized on the structurally unique Ta atom. The LUMO+1 and LUMO+2 are Ta–Ta antibonding in character across the edges of the free Ta_3 face. Figures 8(b) and 8(c) show the frontier MOs of the two Ta_3ZrC_3 isomers **A** and **B**, respectively. For Ta_3ZrC_3 **B**, the HOMO and LUMO orbitals are essentially identical to those in Ta_4C_3 because a Ta atom is the structurally unique metal atom in both species. However, the involvement of the Zr atom in the bonding network of the free metal face has expanded the energy range of the HOMO to HOMO−2. For Ta_3ZrC_3 **A**, there is a slight rearrangement of the occupied frontier MOs compared to Ta_4C_3, yet the energies and energy range of the HOMO to HOMO−2 are similar. The LUMO is also different from that in Ta_4C_3 since the Zr atom now occupies the structurally unique atom site, raising the energy of the MO localized on this atom. Overall, the orbitals show that the Ta_3ZrC_3 **A** and **B** clusters have one less electron in the Ta–Ta/Ta–Zr bonding MOs located over the free metal face, relative to the monometallic Ta_4C_3 cluster.

IV. SUMMARY AND CONCLUSIONS

In summary, bimetallic-carbide clusters of the form Ta_xZrC_y have been generated using a double ablation source. Specific conditions are required for their formation, particularly the relative timing of the ablation events where the downstream Zr rod is ablated before the upstream Ta rod.

PIE spectroscopy was performed on the Ta_3ZrC_y ($y=0-4$) clusters with experimental IEs extracted from the spectra. In comparison to the IE trend for the Ta_4C_y cluster

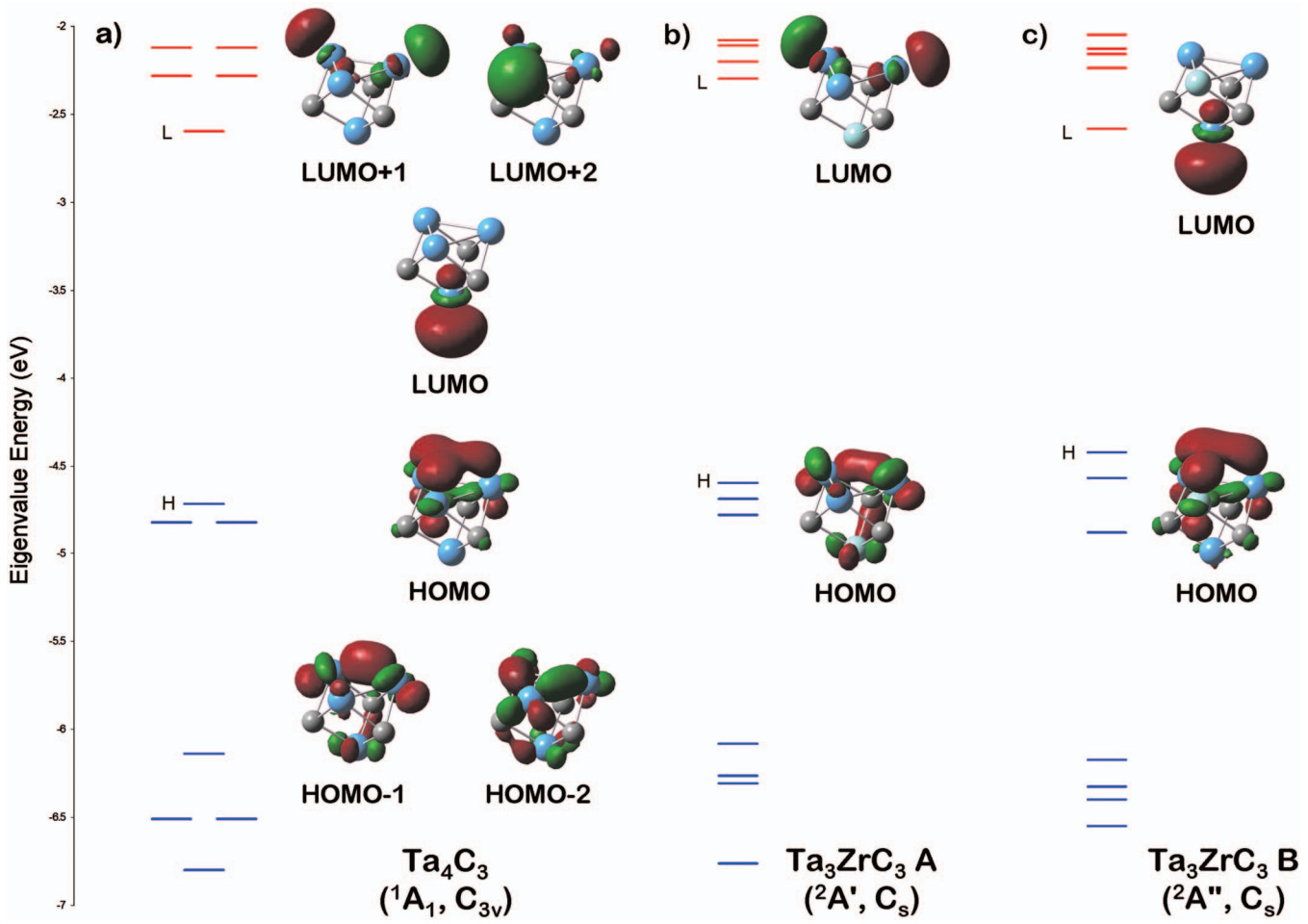

FIG. 8. (Color) Calculated energy level diagrams for the (a) Ta_4C_3, (b) Ta_3ZrC_3 **A**, and (c) Ta_3ZrC_3 **B** clusters. The occupied (unoccupied) orbitals are in blue (red) with the HOMO and LUMO labeled by H and L, respectively. Pictures of the frontier MOs are also shown.

series, the trend for the Ta_3ZrC_y cluster series is reasonably similar, although the IE reductions upon C addition are greater.[15]

DFT calculations were also performed on the possible Ta_3ZrC_y (y=0–4) isomers formed by attaching C atoms to the different metal faces of the tetrahedral Ta_3Zr cluster. The good agreement between the experimental and calculated IE trends indicate that Ta_3ZrC_4 is a $2\times2\times2$ nanocrystal and the smaller clusters exist as fragments of this structure. For Ta_3ZrC, Ta_3ZrC_2, and Ta_3ZrC_3 the lowest energy isomer has all the C atoms bound to the metal faces containing the Zr atom. The slightly favored Zr–C bonding, relative to Ta–C bonding, was reasoned to be due to the greater component of ionic bonding.

Overall this study demonstrates the ability to alter the physical properties of neutral metal-carbide clusters via substitution of a heterometal atom to form bimetallic-carbide clusters. In addition to their intrinsic nanoscale properties, these bimetallic nanocrystals and nanocrystal fragments may also provide useful models for understanding metal-carbide surfaces and their defect sites.

ACKNOWLEDGMENTS

Financial support from the University of Adelaide's Faculty of Sciences is gratefully acknowledged. Support from the Australian Research Council for the purchase and maintenance of our lasers is also acknowledged. Computing resources provided by eResearch SA are also gratefully acknowledged.

[1] M. A. Duncan, J. Cluster Sci. **8**, 239 (1997).
[2] M.-M. Rohmer, M. Benard, and J.-M. Poblet, Chem. Rev. (Washington, D.C.) **100**, 495 (2000).
[3] D. van Heijnsbergen, G. von Helden, M. A. Duncan, A. J. A. van Roji, and G. Meijer, Phys. Rev. Lett. **83**, 4983 (1999); G. von Helden, D. van Heijnsbergen, M. A. Duncan, and G. Meijer, Chem. Phys. Lett. **333**, 350 (2001); C. Oshima, R. Souda, M. Aono, S. Ontani, and Y. Ishizawa, Phys. Rev. Lett. **56**, 240 (1986); C. Oshima, T. Aizawa, M. Wuttig, R. Souda, S. Otani, and Y. Ishizawa, Phys. Rev. B **36**, 7510 (1987).
[4] D. van Heijnsbergen, A. Fielicke, G. Meijer, and G. von Helden, Phys. Rev. Lett. **89**, 013401 (2002).
[5] G. von Helden, D. van Heijnsbergen, and G. Meijer, J. Phys. Chem. A **107**, 1671 (2003).
[6] J. G. Chen, Chem. Rev. (Washington, D.C.) **96**, 1477 (1996).
[7] P. Liu, J. A. Rodriguez, H. Hou, and J. T. Muckerman, J. Chem. Phys. **118**, 7737 (2003).
[8] M. Patzschke and D. Sundholm, J. Phys. Chem. B **109**, 12503 (2005).
[9] S. F. Cartier, B. D. May, and A. W. Castleman, Jr., J. Am. Chem. Soc. **116**, 5295 (1994); J. Chem. Phys. **104**, 3423 (1996); J. Phys. Chem. **100**, 8175 (1996).
[10] S. F. Cartier, B. D. May, and A. W. Castleman, Jr., J. Chem. Phys. **100**, 5384 (1994).
[11] H. Sakurai and A. W. Castleman, Jr., J. Phys. Chem. A **102**, 10486 (1998).
[12] J. Munoz, C. Pujol, C. Bo, J.-M. Poblet, M.-M. Rohmer, and M. Benard, J. Phys. Chem. A **101**, 8345 (1997); M. Benard, M.-M. Rohmer, J.-M.

Poblet, and C. Bo, J. Phys. Chem. **99**, 16913 (1995).
[13] V. V. Ivanovskaya, Y. U. Makurin, A. A. Sofronov, and A. L. Ivanovskii, Russ. J. Phys. Chem. **77**, 695 (2003).
[14] M. W. Heaven, G. M. Stewart, M. A. Buntine, and G. F. Metha, J. Phys. Chem. A **104**, 3308 (2000).
[15] V. Dryza, M. A. Addicoat, J. R. Gascooke, M. A. Buntine, and G. F. Metha, J. Phys. Chem. A **109**, 11180 (2005).
[16] S. Nonose, Y. Sone, S. Onodera, S. Sudo, and K. Kaya, J. Phys. Chem. **94**, 2744 (1990).
[17] M. J. Frisch, G. W. Trucks, H. B. Schlegel *et al.*, GAUSSIAN 03 (Revision D.01), Gaussian, Inc., Wallingford CT, 2004.
[18] D.-S. Yang, M. Z. Zgierski, A. Berces, P. A. Hackett, P. N. Roy, A. Martinez, T. Carrington, Jr., D. R. Salahub, R. Fournier, T. Pang, and C. Chen, J. Chem. Phys. **105**, 10663 (1996); D.-S. Yang, M. Z. Zgierski, and P. A. Hackett, *ibid.* **108**, 3591 (1998).
[19] See EPAPS Document No. E-JCPSA6-131-009925 for energetic and structural information of each respective cluster. For more information on EPAPS, see http://www.aip.org/pubservs/epaps.html.
[20] E. D. Glendening, A. E. Reed, J. E. Carpenter, and F. Weinhold, NBO, Version 3.1.
[21] B. A. Collings, D. M. Rayner, and P. A. Hackett, Int. J. Mass Spectrom. Ion Process. **125**, 207 (1993).
[22] D.-S. Yang and P. A. Hackett, J. Electron Spectrosc. Relat. Phenom. **106**, 153 (2000).
[23] E. Janssens, S. Neukermans, F. Vanhoutte, R. E. Silverans, P. Lievens, A. Navarro-Vazquez, and P. V. R. Schleyer, J. Chem. Phys. **118**, 5862 (2003).
[24] V. Dryza, M. A. Addicoat, J. R. Gascooke, M. A. Buntine, and G. F. Metha, J. Phys. Chem. A **112**, 5582 (2008).
[25] V. Dryza, J. R. Gascooke, M. A. Buntine, and G. F. Metha, Phys. Chem. Chem. Phys. **11**, 1060 (2009).
[26] S. Wei and A. W. Castleman, Jr., Chem. Phys. Lett. **227**, 305 (1994); L. R. Brock and M. A. Duncan, J. Phys. Chem. **100**, 5654 (1996); H. T. Deng, K. P. Kerns, R. Bell, and A. W. Castleman, Jr., Int. J. Mass Spectrom. Ion Process. **167-168**, 615 (1997).
[27] E. Janssens, G. Santambrogio, M. Brummer, L. Woste, P. Lievens, J. Sauer, G. Meijer, and K. R. Armis, Phys. Rev. Lett. **96**, 233401 (2006).
[28] A. Fielicke, C. Ratsch, G. von Helden, and G. Meijer, J. Chem. Phys. **122**, 091105 (2005).
[29] C.-C. Wang, R.-N. Zhoa, and J.-G. Han, J. Chem. Phys. **124**, 194301 (2006).
[30] H. Wang, R. Craig, H. Haouri, J.-G. Dong, Z. Hu, A. Vivoni, J. R. Lombardi, and D. M. Lindsay, J. Chem. Phys. **103**, 3289 (1995).
[31] M. A. Addicoat and G. F. Metha, Aust. J. Chem. **61**, 854 (2008).
[32] *Handbook of Chemistry and Physics*, edited by D. R. Lide (CRC Press, Boca Raton, FL, 1992), p. 10.
[33] H. Harris and I. Dance, J. Phys. Chem. A **105**, 3340 (2001); S. F. Li, X. Xue, Y. Jia, G. Zhoa, M. Zhang, and X. G. Gong, Phys. Rev. B **73**, 165401 (2006); J.-O. Joswig and M. Springborg, J. Chem. Phys. **129**, 134311 (2008).